Accepted Manuscript online: 2022-10-25   Article published online: 2022-11-18

228

**Organic Materials**   O. Chatterjee et al.

THIEME
OPEN
ACCESS

Original Article

Exploring Optically Fueled Dissipative Self-Assembly of a Redox-Active Perylene Diimide Scaffold

Oendrila Chatterjee[a] [ID]
Anup Pramanik[b] [ID]
Apurba Lal Koner* [a] [ID]

[a] Bionanotechnology Laboratory, Department of Chemistry, Indian Institute of Science Education and Research Bhopal, Bhopal By-pass Road, Bhauri, Bhopal 462066, Madhya Pradesh, India

[b] Department of Chemistry, Sidho-Kanho-Birsha University, Purulia 723104, India

* akoner@iiserb.ac.in
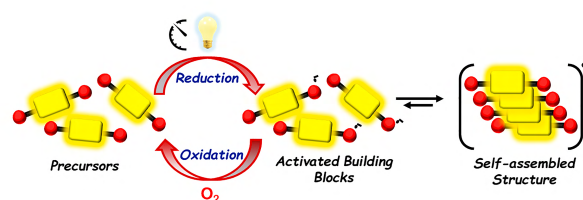
Dedicated to Prof. Francis C. Spano.

Abstract   Dissipative self-assembly is ubiquitous in nature and underlies many complex structures and functions in natural systems. These processes are primarily enabled by the consumption of chemical fuels. However, dissipative self-assembly processes fueled by light have also been parallelly developed, known as optically fueled dissipative self-assembly. Photoswitchable molecules have been widely investigated as prototypical molecular systems for light-driven dissipative self-assembly. Elucidation of optically fueled dissipative self-assembly by a photoresponsive yet non-photoswitchable moiety however remains elusive. This contribution thus demonstrates the first ever report of an optically fueled dissipative self-assembly arising from a redox active perylene diimide scaffold (DIPFPDI). Photo-reduction of neutral DIPFPDI in a poor solvent such as DMF affords its radical anion and repeated irradiation leads to an increased concentration of radical anion, inducing the construction of an H-type aggregate. Nevertheless, dissolved molecular oxygen can efficiently deactivate the radical anions to their neutral precursors and thus the self-assembled state is no longer sustained. The signature of H-type aggregation is deduced from steady-state UV-Vis, fluorescence as well as time-resolved fluorescence spectroscopy. Theoretical insights reveal that dimerization is more feasible in the charged states because of greater delocalization of the excess charge in the charged states. We believe that these findings will infuse new energy into the field of optically fueled dissipative self-assembly of redox-active chromophores.

Key words: radical anions, aggregation, perylene, non-covalent forces, fuel-driven

Introduction

Self-assembly is a unifying parasol for the spontaneous organization of individual components of a system to create an ordered structure, driven by interactions among the components.[1] Non-covalent interactions like H-bonding, dipole–dipole interaction, π–π stacking, van der Waals force, hydrophobic effect, and electrostatic interaction assist in the formation of self-assembled structures. Depending upon the free-energy landscape, the self-assembly process can be classified either as static or dissipative. In static self-assembly, only the building blocks and assembled structure are involved in the assembly process and no energy/matter is whatsoever exchanged with the surroundings.[2] Static self-assembly can either be in equilibrium or kinetic trap, depending on whether the assembly resides in a global or local minima. Unlike static self-assembly, dissipative self-assembly (DSA) relies on a continuous exchange of energy/matter with the external environment to sustain the higher energy assembled state.[3] DSA is ubiquitous in nature, engendering complex structures and functions such as self-healing and homeostasis.[4] Living organisms naturally operate far from thermodynamic equilibrium and represent the fundamental paradigm of DSA.[5] For instance, microtubules in living organisms are assembled from tubulin dimers that are in turn activated by high-energy guanosine triphosphate (GTP).[6] However, once the GTP spontaneously hydrolyses to guanosine diphosphate and orthophosphate, the microtubules can no longer be supported and they disassemble. Thus, continuous consumption of GTP is essential for sustaining the energetically unfavourable assembled state of microtubules. DSA thus emboldens the natural system with the ability of temporal control over the assembled structures, inspiring the development of novel synthetic materials. Thus, over the past several years, the scientific community has been actively involved in the development of synthetic DSA systems.[7] As already stated, DSA systems feature an out-of-equilibrium state attained on perturbing a system upon addition of a fuel. After the pioneering development by van Esch et al.,[8] chemically fueled DSA has witnessed an explosion. Of note, DSA is not limited to relying on only chemical fuel and recent research works have demonstrated that DSA

can also be achieved using light as a fuel. Usage of light as a fuel is not only possible but also offers some advantages over chemically fueled systems such as instantaneous delivery and no waste generation.[9] Till date, optically fueled DSA systems have been illustrated by photoswitchable molecules such as azobenzene.[10] Azobenzene is able to photoswitch between the thermodynamically stable *trans* isomer and the metastable, more polar *cis* form upon UV light exposure. Polar *cis*-azobenzene-functionalized nanoparticles (NPs) self-assemble into spherical aggregates in non-polar solvents. Nonetheless, being inherently unstable they spontaneously convert to the *trans* form. The *trans* form does not support the aggregated state and thus to sustain the NP aggregate, a continuous supply of energy is required.[11] However, demonstration of light-driven DSA by a photo-responsive yet non-photoswitchable chromophore remains elusive. Under this premise, we present herein the first ever demonstration of an optically fueled DSA of a redox active perylene diimide (PDI) derivative. In the plethora of functional dyes, perylene dyes have enthralled scientists due to their outstanding chemical, thermal and photostability in addition to their high extinction coefficients and near unity fluorescence quantum yield.[12] Substitution with six-membered carboxylic imides renders the PDI inherently electron-deficient and qualifies their suitable candidacy for radical-anion generation.[13] Although PDI-based radical anions have been widely utilized in catalysis,[14] organic sensors,[15] magnetic materials,[16] near-infrared (NIR) photothermal materials,[17] and optoelectronics,[18] exploration of its self-assembling properties has been seldom delved into. The present work demonstrates an optically fueled DSA system transpiring from an electron-deficient PDI scaffold (**DIPFPDI**) (Scheme 1). **DIPFPDI** decked with two electron-withdrawing pentafluorophenyl moieties at the *peri*-position is a suitable radical-anion-generating template. Photo-reduction of neutral **DIPFPDI** in a poor solvent such as DMF affords its radical anion, activating it towards self-assembly. The activated

building blocks can also be re-oxidized to their neutral precursors by the dissolved oxygen, leading to their deactivation. Repeated photo-irradiation leads to an increasing concentration of radical anions, inducing the formation of an H-type aggregate. Visible light thus acts as a fuel, modifying neutral precursors into activated building blocks and triggering their self-assembly. When the extent of self-assembly is lesser, the deactivation pathway is efficient, reflecting a dissipative system. However, as the irradiation time elapses, an extended aggregate formation results in the formation of a kinetically trapped system. Theoretical investigations reveal that as a result of greater delocalization of the excess charge in the anionic and dianionic states compared to neutral, dimerization is more feasible for the charged states. The slip-stacked geometry of the neutral dimer transforms into parallel π-stacking interaction for the charged dimers, characterizing the H-type aggregate.

The self-assembly is also governed by solvent polarity and thus it fails to show up in a less polar solvent such as THF. Steady-state UV-Vis–NIR spectroscopy, fluorescence spectroscopy as well as time-resolved fluorescence spectroscopy (time-correlated single photon counting, TCSPC) were carried out to elucidate the photo-reduction-based self-assembly of **DIPFPDI**. Electron paramagnetic resonance (EPR) analysis unequivocally confirmed the radical character of the self-assembled structure. Geometry optimization of neutral **DIPFPDI**, radical anionic species and their corresponding dimers was performed with density functional theory (DFT). Time-dependent DFT (TDDFT) calculations aided in identifying the electronic transitions associated with both the neutral and charged states (anion and dianion) of **DIPFPDI**. Resorting to time-course SEM (scanning electron microscopy) experiment aids one to visualize different morphologies at different irradiation times. Cyclic voltammetry was carried out to gain insight into the electrochemical property of **DIPFPDI**. Spectroelectrochemical analysis of **DIPFPFI** was conducted to identify the spectro-
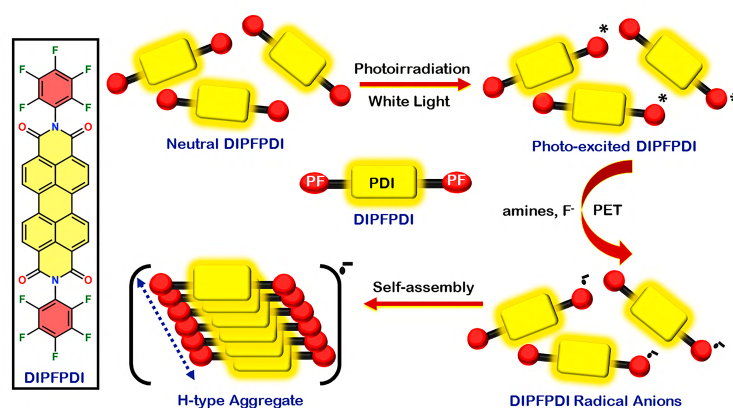
Scheme 1   Mechanism of the radical-anion-mediated self-assembly of **DIPFPDI** involving a photo-induced electron transfer (PET) process.

scopic signatures of **DIPFPDI** upon its electrochemical reduction and thereby confirm the single-electron transfer process.

Results and Discussion

Synthesis of DIPFPDI

DIPFPDI was synthesized following the literature-reported protocol.[19] For the detailed synthetic procedure, see the Supporting Information (SI, Scheme S1). The final product was characterized by ^{1}H NMR and HRMS (Figure S1 and S2).

Optical Properties of DIPFPDI

DIPFPDI exhibits an absorption spectrum characteristic for monomeric PDI dyes, with a main absorption band at 526 nm corresponding to the S_0–S_1 electronic transition (SI, Figure S3a). Additional absorption bands at 490 and 458 nm represent vibronic progressions of the main absorption band arising from coupling of electronic transition and symmetric vinyl stretching mode at 1400 cm^{-1}.[20] The weak absorption in the range of 350–400 nm can be assigned to the S_0–S_2 transition of the perylene core.[21] Excellent overlap of the absorption and excitation spectra confirms the optical purity of **DIPFPDI** while a mirror-image relationship of absorption and emission spectra reflects its rigid backbone. The core rigidity of **DIPFPDI** is evident from its solid-state absorption spectrum, with an absorption maximum at 470 nm accompanied by noticeable vibrational features (Figure S4a). The solid-state emission spectrum of **DIPFPDI** also displays a structured emission (λ_{max} = 675 nm, λ_{ex} = 500 nm), emitting bright red fluorescence with an absolute quantum yield of 0.86% (Figure S4b). Moreover, the remarkable photostability of **DIPFPDI** (SI, Figure S3b) in CHCl$_3$ corroborates its potentiality for visible light-assisted radical anion generation. To investigate the solvent-dependent behaviour of **DIPFPDI**, solvent-dependent absorption and emission spectra were recorded in solvents of varying polarity. In general, the maxima as well as vibronic progressions of the absorption (SI, Figure S5a) and emission spectra (SI, Figure S5b) are only weakly influenced by solvent polarity. One can observe a relatively lesser absorbance of **DIPFPDI** in non-polar toluene and highly polar DMF as compared to solvents of intermediate polarity like CHCl$_3$, DCM and THF. For CHCl$_3$ (Figure S6a), THF (Figure S6b) and DMF (Figure S6c), a linear relationship of absorbance and concentration is maintained till 20 μM, whereas for toluene, the linearity holds up to 15 μM (Figure S6d). Thus, it can be inferred that the aggregation concentration of **DIPFPDI** in DMF is above 20 μM and that in toluene is above 15 μM. Thus, the decrease of absorbance in DMF and toluene is due to a

change in solvent polarity and not due to aggregation. In accordance with the trend observed in absorption, emission intensity of **DIPFPDI** is also decreased in toluene and DMF.

Elucidating Optically Fueled Self-Assembly of Photo-reduced DIPFPDI

Temporal Evolution of Absorption Spectra

For probing radical anion generation from **DIPFPDI**, the obvious solvent choice was DMF as intrinsically generated dimethyl amines are known to effectually reduce electron-deficient moieties. Such reduction proceeds via a facile electron transfer process from the HOMO of donor to the LUMO of acceptor. Concentration-dependent studies of **DIPFPDI** in DMF reveal a linear relationship of absorbance and concentration until 20 μM, beyond which deviation from linearity suggests onset of aggregation (Figure 1a). The intensity ratio of the vibronic progressions (A_{0-0}/A_{0-1}) is often used to approximate the extent of intermolecular excitonic coupling in perylene dyes.[22] Gratifyingly, the A_{0-0}/A_{0-1} ratio (1.56) extracted from the absorption spectra of **DIPFPDI** in DMF (c = 20 μM) (Figure 1b) is in accordance with the value reported for monomeric perylenes. Figure 1c represents the temporal evolution of **DIPFPDI** absorption profile in DMF upon visible light irradiation in a photo-reactor (illuminance ~970 lx). Upon photo-irradiation, vibronic progressions in-
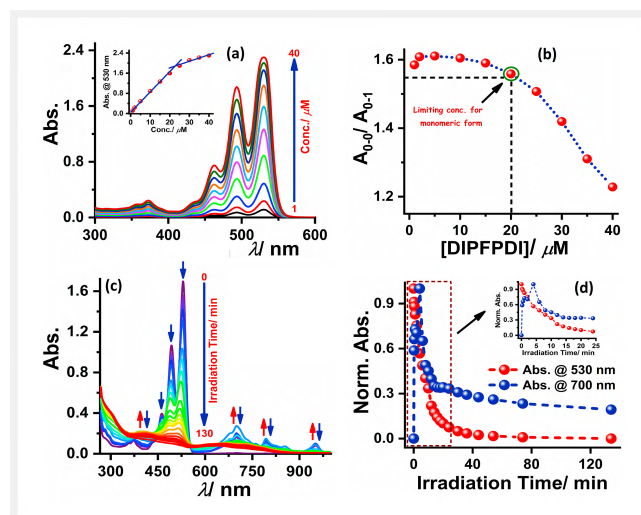

Figure 1 (a) Concentration-dependent absorption spectra of **DIPFPDI** in DMF; inset: change of absorbance at 530 nm against concentration. (b) Intensity ratio of vibronic progressions (A_{0-0}/A_{0-1}) against concentration. (c) Temporal changes in the absorption profile of **DIPFPDI** (20 μM) in DMF with visible light irradiation. Arrows indicate the spectral changes upon increasing irradiation time. (d) Changes in normalized absorbance at 530 and 700 nm against irradiation time; inset: zoomed-in view of the changes in normalized absorbance with increasing irradiation at shorter time scale. All measurements were acquired using quartz cuvettes of 1 cm pathlength.

231

Organic Materials   O. Chatterjee et al.   THIEME OPEN ACCESS   **Original Article**

herent to neutral **DIPFPDI** rapidly diminished with concomitant appearance of several new absorption bands spanning across the entire UV-Vis–NIR region. The absorption spectrum of **DIPFPDI** radical anion displays three new peaks at 700, 792 and 952 nm, which are characteristic of D_0–D_n transitions of radical anion.[23] These peaks constantly grow in intensity till 4 min of irradiation, beyond which they decrease and coalesce to give a broad absorption profile. Such merging of vibrational fine structures signifies intermolecular excitonic coupling and insinuates towards the self-assembly process. A close analysis of Figure 1c reveals a prominent decrease in the ratio of intensities of the 0–0 and 0–1 bands (A_{0-0}/A_{0-1}), from 1.68 (at 0 min) to 0.75 (at 130 min), implying a strong H-type excitonic coupling (SI, Figure S7).[24] This is also coupled with an appreciable hypsochromic shift (15 nm) of the vibronic progressions and an increase in exciton bandwidth from 71.7 to 131 meV.[25] Of note, during the course of photo-reduction, H-promoting excitonic coupling leads to transfer of oscillator strength to 0–3 vibronic band and eventually to that of the S_0–S_2 regime. Thus, the trace at 700 nm is perceived as a growth and decay profile; the growth corresponds to the piling up of **DIPFPDI** radical anion and the decay reflects their H-type coupling (Figure 1d). However, in the absence of visible light irradiation, the system remains unperturbed, thus affirming that a photo-induced electron transfer (PET) is in progress to engender an optically fueled self-assembling template (SI, Figure S8). In order to confirm the photo-reduction mechanism mediated by the residual amines in DMF, we also followed the temporal changes in the absorption profile of **DIPFPDI** using triethylamine as the sacrificial agent. Photo-reduction occurred here too, and the results are in agreement with those obtained in DMF (SI, Figure S9). Cyclic voltammetry was conducted to understand the electrochemical property of **DIPFPDI** (Figure S10a). Spectroelectrochemical analysis of **DIPFPDI** was conducted using nonbasic Bu_4NPF_6 as a supporting electrolyte. On application of negative potential (−1.0 V) to **DIPFPDI**, the absorption maxima at 530 nm corresponding to neutral species steadily decreases and a new spectrum emerged with characteristic peaks at 700, 760 and 790 nm. Thus, this excellent correlation between electrochemical and chemical reduction suggests that the said reduction of **DIPFPDI** is essentially a one-electron transfer process evading any covalent bond formation (SI, Figure S10b). Having established the light-driven self-assembly of photo-reduced **DIPFPDI**, we then embarked upon unravelling the very nature of this self-assembly. Light is used here for external intervention, for photo-exciting neutral precursors into the photo-excited state, which is a better oxidant.[14a] Electron transfer then takes place from the amines present in DMF to photo-excited **DIPFPDI**, forming radical anions. Once the neutral precursors are activated into its radical anionic counterpart (the activated building blocks), they begin to construct a self-assembled structure, H-type

aggregate to be precise (Scheme 2). Since photo-reduction is a chemical process requiring the involvement of a chemical fuel (amines present in DMF) jointly with light, the system studied herein is different from conventional optically fueled systems demonstrated by photoswitchable moieties. Now, the activated building blocks can also be deactivated to their neutral precursors via their re-oxidation, mediated by the dissolved molecular oxygen present in DMF. When the activated building blocks are thus deactivated to their neutral precursors, the assembled state can no longer be sustained and the aggregates fall off. Consecutive intervals of irradiation of **DIPFPDI** led to an increasing population of its radical anion and re-oxidation by molecular oxygen competes with the photo-reduction pathway. Thus, for different irradiation intensity and time, depending upon the concentration of neutral/radical anion species present, one can have access to different equilibrium situations and thereby of the H-aggregates being formed. In order to probe the temporal response of self-assembly, we took recourse to an oxidizing agent, nitrosyl tetrafluoroborate ($NOBF_4$). A solution of **DIPFPDI** photo-irradiated for 0.5 min and then treated with 1 equiv of $NOBF_4$ regenerates the original **DIPFPDI** spectrum (SI, Figure S11a). Contrarily, the solution of **DIPFPDI** photo-irradiated for 130 min does not regenerate the original spectrum even after being treated with 10 equiv of $NOBF_4$ (SI, Figure S11b). This implies that when extent of aggregation is lesser, $NOBF_4$ can efficiently re-oxidize the radical anion leading to easier disassembly. However, it fails to do so once interchromophoric interactions gives rise to a kinetically trapped extended H-type aggregate formation. Upon being photo-irradiated for 4 min, the aggregate that formed could be efficiently deactivated via re-oxidation by molecular oxygen. Hence, upon removal of the fuel source, the deactivation reaction could be rapidly completed in a time span of 36 min (Figure 2a). Different from the optically fueled dissipative systems concerning photoswitchable moi-

Scheme 2   Light-driven dissipative self-assembly of photo-reduced DIPFPDI.

eties, the deactivation reaction here generates the products of molecular oxygen reduction as wastes. In contrast, when **DIPFPDI** is photo-irradiated for 12 min, the efficiency of the deactivation mechanism is reduced due to the formation of an extended H-aggregate that becomes kinetically trapped (Figure 2b). Thus, a slower decrease of the absorbance at 700 nm for a 12-min irradiated sample compared to a 4-min one is due to the greater extent of self-assembly in the former (Figure S12). For a dissipative system, aggregation of activated building blocks can often alter the rate of energy dissipation and exert negative feedback on the oxidation. In a dissipative system, when used in a large amount, the fuel can often navigate the self-assembled structures into a kinetic trap and thus suppress the deactivation pathway.[26] Diffusion of molecular oxygen into the extended aggregate being low, the efficiency of deactivation is reduced leading to kinetic trapping. Thus, as the irradiation time elapses, the dissipative kind of state gradually transforms to a kinetically trapped one. In order to help the system escape the kinetic trap, we followed the deactivation reaction in a solvent mixture of $CHCl_3$ (a good solvent) and DMF (Figure S13). Although the deactivation reaction is improved upon the addition of $CHCl_3$, the kinetically trapped state could not be completely escaped. To confirm molecular oxygen as the pertinent species responsible for the deactivation pathway, the deactivation reaction was also followed in an inert (N_2-purged) solution (Figure 2c,d). On comparing the radical anion decay kinetics in a N_2-purged solution compared with

those of an air-saturated and an oxygen-purged solution, we find that the decay kinetics proceeded fastest in an oxygen-purged condition, followed by the air-saturated and nitrogen-purged ones, respectively (Figure 3a). This revivifies the fact that the dissolved oxygen indeed re-oxidizes the generated radical anion and governs the deactivation step. Thus, the total irradiation time required to reach the extended H-aggregate formation stage in a N_2-purged solution is much greater than that in an air-saturated solution (250 vs. 130 min) for solutions of same concentration irradiated with similar light intensities (SI, Figure S14). Alternation of photo-irradiation between an 'ON' (fueled for 4 min) and an 'OFF' (fuel source suspended for 36 min) state allowed **DIPFPDI** to toggle between its negatively charged and electrically neutral state, exhibiting a reversibly switchable nature (Figure 3b,c). To explain the fatigue effect in the consecutive cycles of the reversibility scan, we resorted to kinetic experiments. In the first instance, we followed the time evolution of **DIPFPDI** immediately after oxidation (Figure 3d). A rapid decay of absorbance at 700 nm confirmed re-oxidation if any. In the second instance, **DIPFPDI** obtained after 1 redox cycle and then kept 1 h for seeding were added to the solution of just-cycled **DIPFPDI**. One can observe that there is a long growth phase reflecting nucleation prior to the commencement of decay. When sonicated seeds were used, one observes an even slower moving decay trace. Thus, the reason behind the fatigue effect is the formation of nuclei that do not completely disassemble, implying a memory ef-
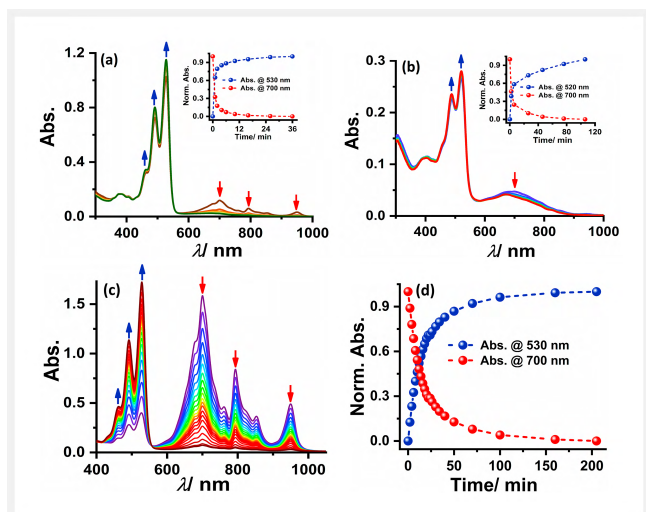

Figure 2 Temporal response of the deactivation reaction in an air-saturated solution of DMF after optical fueling for (a) 4 min; inset: corresponding changes in the normalized absorbance at 530 and 700 nm, and (b) 12 min; inset: corresponding changes in the normalized absorbance at 520 and 700 nm. (c) Temporal response of the deactivation reaction in an inert (N_2-purged) solution of DMF after optical fueling for 4 min and (d) corresponding changes in the normalized absorbance at 530 and 700 nm. All measurements were acquired using quartz cuvettes of 1 cm pathlength.
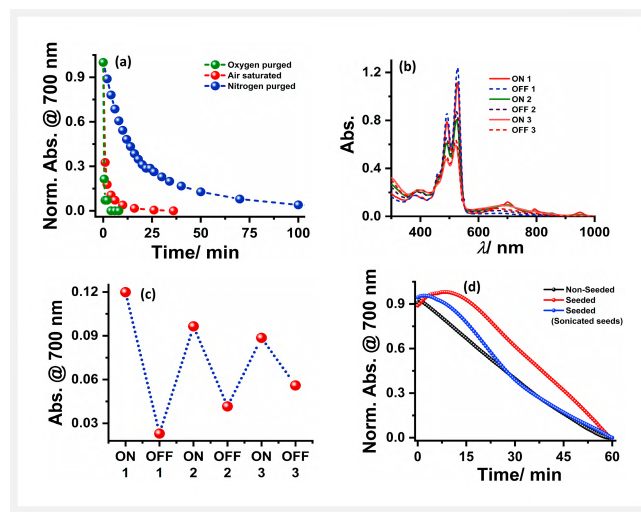

Figure 3 (a) Comparison of the radical anion decay kinetics in an oxygen-purged, air-saturated and nitrogen-purged solution of DMF. (b) Renewable absorption spectra of **DIPFPDI** upon alternation of photo-irradiation between an 'ON' (fueled for 4 min) and an 'OFF' (fuel source removed for 36 min) state and (c) corresponding changes in absorbance at 700 nm, exhibiting a switchable nature. (d) Normalized absorbance at 700 nm vs. time after 1 redox cycle for 20 µM **DIPFPDI** (black trace) and for 20 µM **DIPFPDI** seeded with 1 h aged seeds (red trace) and sonicated seeds (blue trace).

fect. As seen from Figure S15, the rate of photo-reduction of **DIPFPDI** when measured as a function of the irradiation time proceeds fastest for 20 µM, followed by 5 and 2 µM, respectively. Since re-oxidation by dissolved oxygen competes with the photo-reduction, the H-type aggregate so constructed is composed not only of the photo-reduced species but also of the neutral precursors. Hence, under the effect of identical light intensities, for a more concentrated sample, greater predominance of the neutral species leads to a faster self-assembly. Thus, the kinetics of optically fueled self-assembly exhibit a strong concentration dependence. To further investigate the effect of light intensity on the light-driven self-assembly, the time course of the self-assembly was monitored under two different light intensities (SI, Figure S16). The irradiation time required for the extended aggregate formation is inversely proportional to the light intensity used, thus allowing one to have a temporal control over the system.

Temporal Evolution of Emission Spectra

Radical-anion-mediated self-assembly of **DIPFPDI** could also be inferred from the temporal changes in its emission profile. Concentration-dependent emission spectra testify H-promoting excitonic coupling for **DIPFPDI**, as inferred from a decrease in the ratio of intensities of 0–0 and 0–1 bands (I_{0-0}/I_{0-1}) (Figure 4a). Figure 4b summarizes the temporal evolution of the **DIPFPDI** emission profile with optical fueling. The emission spectrum of neutral **DIPFPDI** exhibits characteristic vibronic progressions of S_0–S_1 electronic transition at 546, 585, and 635 nm. Upon subjecting **DIPFPDI** to visible-light exposure, photo-reduction occurred whereby the vibronic progressions innate to neutral **DIPFPDI** rapidly diminished, signifying the PET mechanism. Diminution in intensity of the vibronic bands along with their merging symbolizes intermolecular excitonic coupling. The PL ratio also monotonically decreases with increasing photo-reduction, mirroring the H-type excitonic coupling (SI, Figure S17). Moreover, concomitant enhancement of emission intensity in the lower wavelength region (410–480 nm) is reminiscent of H-type aggregation. It is worth mentioning that no such spectral changes are registered for the solution without photo-reduction, thus endorsing the optically fueled self-assembling propensity of **DIPFPDI** (Figure 4c). Excitation spectra recorded for the higher (λ_{em} = 410, 435, 462 nm) and lower energy (λ_{em} = 558 nm) domains of photo-reduced **DIPFPDI** differed considerably, indicative of ground-state aggregation (Figure 4d). It is worth mentioning that if the excitation spectra at different monitoring wavelengths resembled one another, it would imply an excited-state phenomenon and would dissuade the ground-state self-assembly process. Temporal evolution of emission spectra for different concentrated solutions of **DIPFPDI** follows similar profiles (Figure S18a, b); however, the rate of decrease of emission intensity is fastest for 30 µM followed by
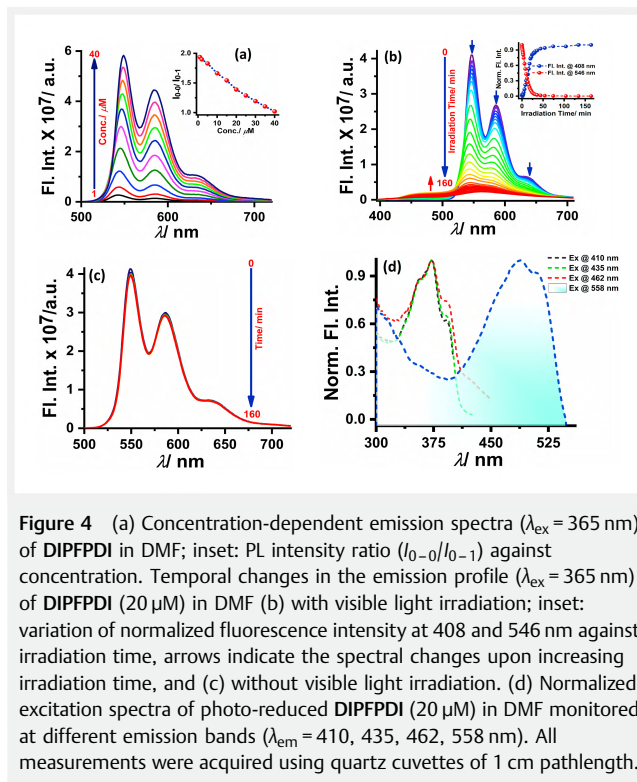

Figure 4 (a) Concentration-dependent emission spectra (λ_{ex} = 365 nm) of **DIPFPDI** in DMF; inset: PL intensity ratio (I_{0-0}/I_{0-1}) against concentration. Temporal changes in the emission profile (λ_{ex} = 365 nm) of **DIPFPDI** (20 µM) in DMF (b) with visible light irradiation; inset: variation of normalized fluorescence intensity at 408 and 546 nm against irradiation time, arrows indicate the spectral changes upon increasing irradiation time, and (c) without visible light irradiation. (d) Normalized excitation spectra of photo-reduced **DIPFPDI** (20 µM) in DMF monitored at different emission bands (λ_{em} = 410, 435, 462, 558 nm). All measurements were acquired using quartz cuvettes of 1 cm pathlength.

15 and 5 µM (Figure S18c). Thus, light-driven self-assembly of photo-reduced **DIPFPDI** also reveals concentration dependence in their emission profiles, similar to that deduced from absorption studies.

Rationalization of H-Type Aggregation from Fluorescence Decay Profiles

Optically fueled self-assembly of photo-reduced **DIPFPDI** was also monitored using the TCSPC technique. The fluorescence decays of photo-reduced **DIPFPDI** in DMF were measured by excitation with a 509 nm diode laser, and the decay of the vibrational progressions of the S_0–S_1 emission spectrum was monitored (Figure 5a–c).
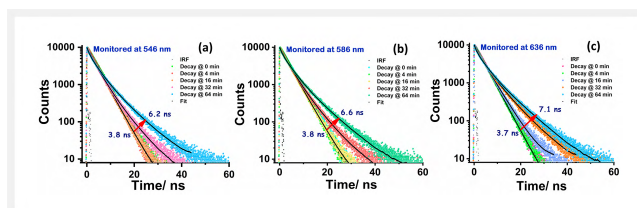

Figure 5 Fluorescence decay profiles (λ_{ex} = 365 nm) of **DIPFPDI** (20 µM) in DMF monitored as a function of irradiation time at (a) 546 nm, (b) 586 nm and (c) 636 nm emission bands. All measurements were acquired using quartz cuvettes of 1 cm pathlength.

Neutral **DIPFPDI** exhibited bi-exponential fluorescence decay at 546 nm emission band with a decay time of 3.8 ns, typical for the neutral singlet excited state of monomeric PDI. Upon photo-irradiation for 4 min, the decay is still bi-exponential with a slight increase in the time constant of the shorter lifetime species. Upon photo-irradiation for 16 min, the contribution of the monomer drops (100% to 93%) Additionally, the presence of a species with a lifetime of 0.9 ns perhaps signifies the presence of non-radiative decay pathways in aggregates (Table 1). With further irradiation (32 and 64 min), the traces could only be fit to a tri-exponential decay. The faster decay component with a sub-nanosecond lifetime persists at all irradiation times. The amplitude of the monomeric component eventually drops from 93% to 43% and its time constant decreases from 3.8 to 3.4 ns. Eventually, species with a longer lifetime appears, whose amplitude increases from 27% to 50% and the time constant increases from 6.6 to 7.4 ns. Such species with enhanced excited-state lifetime are typical for systems with H-promoting excitonic coupling. For an H-type excitonically coupled system, enhancement in the excited state lifetime occurs as the radiative transition to the ground state from the lowest excited state is optically forbidden.[27] Similar trends were noted for the 586 and 636 nm emission bands (SI, Tables S1 and S2).

Table 1 Time-resolved fluorescence decay parameters of 546 nm emission band as a function of irradiation time[a]

Irradiation time (min)	τ_1 (ns)	α_1	τ_2 (ns)	α_2	τ_3 (ns)	α_3	τ_{avg}[b] (ns)	χ^2
0	3.8	98	0.4	2	–	–	3.8	1.2
4	3.8	98	0.7	2	–	–	3.8	1.2
16	3.8	93	0.9	7	–	–	3.7	1.2
32	3.5	66	0.7	7	6.6	27	4.8	1.1
64	3.4	43	0.6	7	7.4	50	6.2	1.1

[a]λ_{ex} = 373 nm, the decay times (τ_1, τ_2, and τ_3), the respective fractional contributions (α_1, α_2, and α_3), the weighted average decay time (τ_{avg}) and the quality of fitting are shown. [b]Error values are less than 5%.

Role of Solvent in Tuning Aggregation

Solvent polarity can often govern the self-assembly of π-conjugated molecules. Thus, we aimed at elucidating the role of solvent polarity in directing the self-assembly of photo-reduced **DIPFPDI**. For this purpose, we took recourse to the less polar solvent THF, using TBAF (tetra-butyl ammonium fluoride) as the external reductant. In contrast to the PET pathway in DMF, the thermal electron transfer pathway is turned 'ON' in THF. Depending on the relative energy levels of HOMO and LUMO, either of the PET or thermal electron transfer pathway is turned 'ON'.[28] Upon thermal electron transfer in THF in the presence of TBAF as a donor, vibration-

al fine structures of neutral **DIPFPDI** steadily diminished with concurrent appearance of new absorption peaks spanning the UV-Vis–NIR region, characterizing the transitions of radical anion species (Figure 6a). However, in contrast to DMF, here in THF, no intermolecular excitonic coupling was evident, inferred from the intact vibrational fine structures. Moreover, the absorption features in the S_0–S_2 regime remained intact. This is because the absorption corresponding to S_0–S_2 transition of neutral **DIPFPDI** is close to a deep-lying spin-allowed transition of the **DIPFPDI** radical anion (vide infra). Temporal changes in the emission profile revealed a rapid quenching of fluorescence intensity in the S_0–S_1 regime, correlating to the transformation from neutral to radical anion state. Nonetheless, the emission intensity from the S_2 state remained unperturbed (Figure 6b). Excitation spectra at different monitoring wavelengths resemble distinct regions of the absorption spectra, consistent with the emission emanating from both S_1 and S_2 electronic states (Figure 6c). Note that the excitation spectrum at λ_{em} = 576 nm mirrors monomeric perylene and thus clearly rules out the possibility of any aggregation. Presence of the **DIPFPDI** radical anion manifests as a diminution of the monomeric S_1 emission. Thus, the fluorescence decay profiles are mono-exponential in nature with a decay time of about 3.8 ns for the S_1 state (Figure 6d). The mono-exponential decay profile evinces the presence of monomeric **DIPFPDI** radical anion. Thus, it can be deduced that the sol-
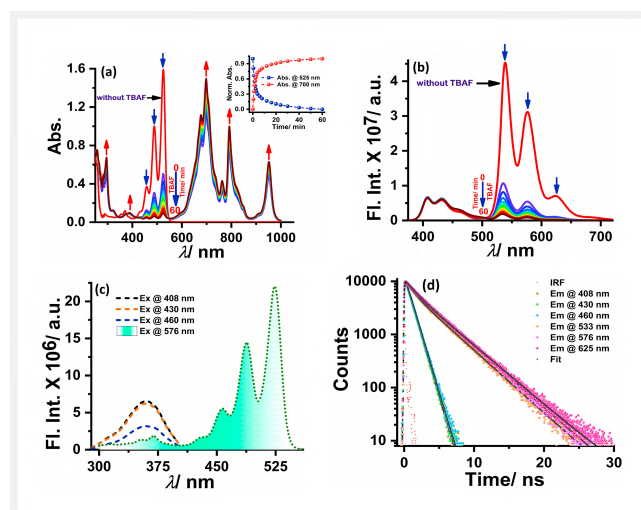

Figure 6 Temporal changes in the (a) absorption and (b) emission profiles (λ_{ex} = 365 nm) of **DIPFPDI** (20 μM) upon reduction in THF with TBAF as the reductant. The arrows indicate the spectral changes with time. (c) Excitation spectra of reduced **DIPFPDI** (20 μM) in THF monitored at different emission bands (λ_{em} = 408, 430, 460 and 576 nm). (d) Fluorescence decay profiles of **DIPFPDI** (20 μM) obtained in the THF/TBAF system at different emission bands (λ_{em} = 408, 430, 460, 533, 576 and 625 nm). All measurements were acquired using quartz cuvettes of 1 cm pathlength.

vophobic effect in polar DMF drives the self-assembly of photo-reduced **DIPFPDI**.

Validation of the Radical Character of DIPFPDI via EPR Spectroscopy

To substantiate the radical character of **DIPFPDI**, EPR measurements were conducted. Obtained EPR signals verified the radical character of **DIPFPDI**. The broadened EPR signal in DMF indicates the radical-based self-assembly of **DIPFPDI** (Figure 7a),[29] corroborating with the spectroscopic results. However, in THF the EPR signal is sharp, as expected for monomeric radical anion (Figure 7b). The **DIPFPDI** radical anion in DMF gave a resonance signal at 3460 G with a g-factor of 1.94. On the other hand, the resonance signal at 3480 G in THF gives rise to a g-factor of 1.93.
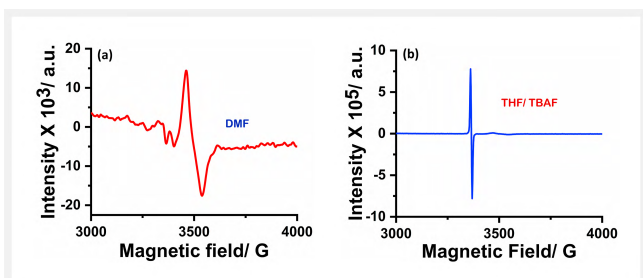

Figure 7   EPR spectra of **DIPFPDI** (20 μM) in (a) DMF and (b) THF/TBAF system at −173 °C

Insight into the Theoretical Investigations

For understanding the spectral feature and in order to provide a deeper insight into the mechanism of aggregate formation, we performed theoretical investigations on **DIPFPDI** both in the neutral and anionic states. Geometry optimizations were performed for neutral **DIPFPDI**, radical anionic species and the corresponding dimers using DFT methodologies as implemented in Gaussian 16.[30] We used long-range-corrected density functional, CAM-B3LYP along with 6–311 G** basis sets for all the atoms. The optimized geometries of the species are shown in SI (Figure S19). As evidenced, the terminal pentafluorophenyl rings occupy a cross-orientation with respect to the planar PDI moiety, both in the neutral and anionic forms. Remarkably, the dihedral angle (ϕ) between the plane of PDI and the substituted phenyl rings decreases with increasing the charge (ϕ = 77.4, 73.4, and 70.0 degrees, respectively, for neutral, anionic, and dianionic species). This indicates that the excess charge is more prone to be shared by the phenyl rings, thereby increasing the degree of conjugation. We have computed the possibility of all probable dimer formation by exploring

their formation energy (Figure 8). The neutral dimer has the formation energy −4.32 kcal/mol, while the corresponding radical anion and dianion have much greater formation energy, −12.93 and −29.21 kcal/mol, respectively. Thus, formation of charged dimers (anionic and dianionic) is much favoured compared to its neutral analogue. As the radical anion experiences more delocalization involving the PDI and the terminal phenyl rings, thus it is more susceptible to form an aggregate. The neutral dimer adopts a slip-stacked geometry, slipped along the short molecular axis, entitled as Hj-type aggregate.[31] However, both kinds of charged dimers (anionic and dianionic) indicate parallel π-stacking interaction, characteristic of H-type aggregation. The PDI planes in the charged dimers are separated by almost 6.5 Å, while the intermolecular F–F distance (of the pentafluorophenyl rings) is about 2.8 Å. For computing the spectral features of the species, we performed TDDFT calculations in the DMF medium by employing a polarizable continuum model using the integral equation formalism variant (IEFPCM). It has been reported that the use of hybrid functional produces better optical properties for polyatomic hydrocarbons.[32] Thus, we employed the Heyd–Scuseria–Ernzerhof exchange correlational functional (HSE06) for computing the absorption spectra.[33] As shown in Figure 9a, the neutral **DIPFPDI** shows a strong absorption centered at 516 nm (oscillator strength, f = 0.97), which is in excellent agreement with the experimental value (530 nm). The transition is characterised to be the band-gap absorption where both the HOMO and LUMO reside on the PDI moiety (see SI, Figure S20). Another low-intensity absorption located around 340 nm (oscillator strength, f = 0.09) originates from the deep-lying state
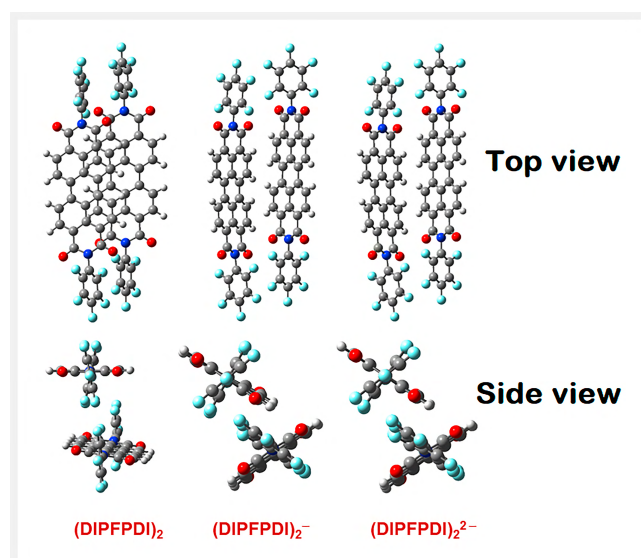

Figure 8   Optimized geometries of **DIPFPDI** dimers in neutral, radical anionic and dianionic states. The top panel represents their side view, whereas the bottom panel represents the top view.
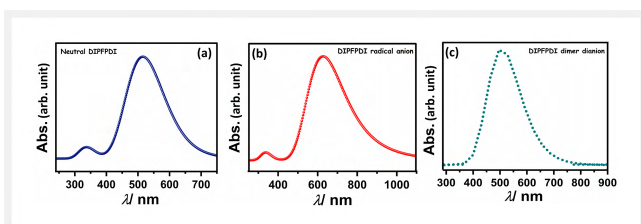
Figure 9 Calculated absorption spectra of **DIPFPDI** for the (a) neutral state, (b) radical anionic state, and (c) dimer dianionic state.

(HOMO-4) to the LUMO orbital. The low intensity of that transition might be attributed to the poor overlap between the HOMO-4 and the LUMO orbital as because the former is situated on a substituted phenyl ring. These two transitions are assigned to be the experimental S_0–S_1 and S_0–S_2 transitions, respectively. The radical anion shows the most intense absorption at around 620 nm (oscillator strength, $f = 1.03$) with additional low-intensity absorptions in the range of 700–830 nm (oscillator strength, $f = 0.05$–0.06) (Figure 9b). The most intense absorption is characterized to be spin-allowed from the singly occupied molecular orbital to the next orbital. Additionally, the low-intensity absorption at 340 nm is a spin-allowed transition from the deep-lying doublet state. Both radical dimers, anion (SI, Figure S21) and dianion (Figure 9c), characterize a strong absorption (oscillator strength = 1.21) at 538 and 502 nm, respectively. Molecular electrostatic potential maps provide information about the electron donor and electron acceptor regions (Figure 10). Different values of the electrostatic potential surface at the molecular surface are represented by different colours. The red colour represents the region with the minimum electrostatic potential signifying excess electrons and acts as an electrophilic attack. The blue region indicates the maximum of electrostatic potential, and it acts opposite. For neutral **DIPFPDI**, one can observe a predominance of blue regions corroborating its electron-deficient nature. Upon single-electron transfer, neutral **DIPFPDI** is converted to its radical
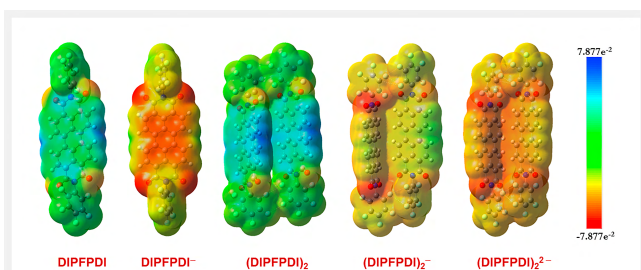

Figure 10 Molecular electrostatic potential maps of **DIPFPDI** in neutral monomer, monomer radical anion, neutral dimer, dimer radical anion and dimer dianion states (electrostatic potential contours are colour-coded from red (negative) to blue (positive) and are in the range from −7.877 a.u. (red) to +7.877 a.u. (blue).

anion and thus the red regions mostly settle upon the carbonyl oxygen atoms. The excess negative charge is easily delocalized throughout the perylene backbone and hence the core now assumes red colour.

Microscopic Investigation of Self-Assembly

SEM conducted in a time-dependent fashion evinces the morphological transformation occurrent upon photo-reduction-assisted self-assembly. The time-course SEM images represent static snapshots of the system corresponding to different H-aggregates under different equilibrium conditions, depending upon the concentration of neutral/radical anionic species present. The nascent solution composed of only neutral **DIPFPDI** in DMF adopts a dispersed particle-like morphology as shown in Figure 11a. Upon 4 min of visible light exposure, the initially dispersed particles yield twisted fibres (Figure 11b). Further, at 16 min of irradiation, unwinding of the twisted fibres yield microfibres (Figure 11c). These microfibres initiate further unyolking to ultimately form spherical particles (Figure 11d).
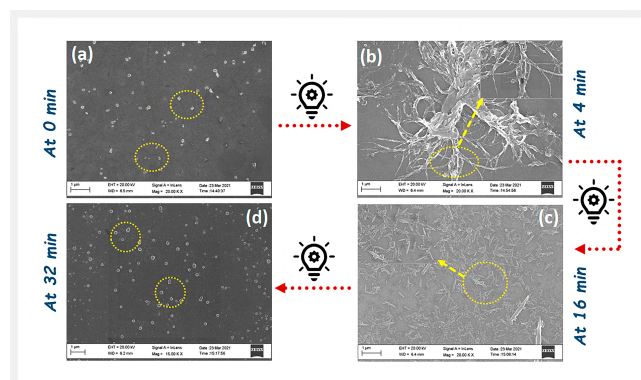

Figure 11 Morphological evolution during optically fuelled self-assembly of **DIPFPDI** (20 μM) in DMF. (a) Dispersed particle like morphology of the nascent solution. (b) Twisted fibres upon 4 min of irradiation and the inset shows the zoomed-in view of the twisted fibres. (c) Unwinding of the twisted fibres upon 16 min of irradiation and the inset shows the zoomed-in view of the unwinding. (d) Disassembly occurs to yield spherical particles.

Conclusions

The work presented herein demonstrates optically fueled DSA of a non-photoswitchable yet photo-responsive system for the first time. In presence of visible light, neutral **DPFPDI** is efficiently converted into its radical anion and repeated irradiation triggers the construction of an extended H-type aggregate. Visible light thus acts as a fuel, modifying a neutral precursor into radical anions which act as the building

blocks for the self-assembly. Nonetheless, the radical anions are spontaneously re-oxidized back to the neutral precursor via the dissolved molecular oxygen and hence the self-assembled state collapses. Theoretical insights show that as a result of greater charge delocalization in the radical state, the formation energy increases as one moves from the neutral dimer to the dimer radical anion and to the dimer dianion. This study thus provides important information in unravelling light-driven DSA of a redox-active system. In addition, the self-assembling propensity in the radical anion state will also shed some light on research pertaining to the stabilization of radical anions.

Experimental Section

Materials and Methods

Chemicals

Spectroscopic-grade chloroform ($CHCl_3$) and DMF were obtained from Sisco Research Laboratories Private Limited and used as received. Anhydrous THF used for spectroscopic measurements was distilled from metallic sodium and benzophenone under nitrogen reflux. Tetra-*n*-butyl ammonium fluoride, 2,3,4,5,6-pentafluoroaniline, *N*-methyl-2-pyrrolidone, and [poly(methyl methacrylate)] (PMMA) used were acquired from Sigma-Aldrich, while acetic acid (AcOH) was obtained from Spectrochem Private Limited.

Instrumentation and Methodology

NMR spectroscopy: ^{1}H NMR spectrum of **DIPFPDI** was recorded on a Bruker 500 MHz spectrometer and the chemical shift determined in ppm unit with respect to the signal of residual solvent ($\delta = 7.26$ ppm).

Mass spectrometry: High-resolution mass spectrum was obtained using the APCI technique on a Bruker Micro-TOF-Q-II mass spectrometer with $CHCl_3$ as the eluent.

Photo-irradiation: Visible light irradiation of **DIPFPDI** was carried out on a Luzchem photo-reactor (LZC-ORG), which houses 10 lamps furnishing side irradiation to the sample. To eliminate the effect of any other external light source, the photo-irradiation was carried out in the photo-reactor placed in a dark room. For the purpose of visible light irradiation, cool white fluorescent lamps (8 W, 390 lumen) were used. The total illuminance as measured by a Lutron LX 101 luxmeter was found to be 970 lx. Intensity variation was performed by reducing the number of lamps. For the purpose of obtaining temporal evolution of absorption and emission spectra, **DIPFPDI** in DMF and THF were photo-irradiated for a specific time interval prior to acquiring any absorption, emission and time-resolved fluorescence measurements. Such repeated photo-exposure time was summed up and interpreted as the total irradiation time.

Steady-state absorption spectroscopy: Steady-state UV-Vis–NIR spectra were acquired on a Shimadzu 1800 spectrophotometer using quartz cuvette of 1 cm path length. For solid-state absorption study, the sample was poured into the sample holder and absorbance measured in a Carry 5000 spectrophotometer using the diffusion reflectance method.

Steady-state fluorescence spectroscopy: Steady-state fluorescence measurements were carried out on Jobin Yvon Fluorolog-3-21 equipped with a 450 W Xenon CW lamp as the excitation source. All the acquired fluorescence spectra were corrected with respect to the excitation light intensity and photomultiplier tube response using the correction files available in HORIBA software. The excitation and emission slits were varied according to the condition of measurements. All the measurements were performed under magic angle conditions (54.7°). Solid-state emission spectra of the sample were measured by keeping the sample holder at a specific angle in the Jobin Yvon Fluorolog.

Time-resolved fluorescence spectroscopy: Time-resolved fluorescence measurements were carried out on a TCSPC spectrometer (Delta Flex-01-DD/HORIBA) under magic angle conditions (54.7°). A Delta diode laser of 373 nm was used as the excitation source and the photon count was set to 10000. A picosecond photon detection module equipped with a Hamamatsu MCP photomultiplier (R-3809U-50) tube was used as the detector. The instrument response function was recorded using an aqueous solution of colloidal silica (Ludox). Decay curves were analyzed by nonlinear least-squares iteration using inbuilt EZtime decay analysis software and the quality of the fitting was then assessed by taking a note of the fitting parameter (χ^2).

Fluorescence quantum yield (QY) determination: The absolute quantum yield of **DIPFPDI** was measured using $BaSO_4$-coated integrating sphere from HORIBA Jobin Yvon attached to Fluorolog. The solid sample was excited at 500 nm and the emission range was fixed in the 510–800 nm region.

EPR spectroscopy: EPR spectra were acquired on a Bruker Biospin Gmbh spectrometer using a microwave frequency of 9.4 GHz at the X-band. The Lande *g*-factor was calculated using the equation: $g = \frac{h\nu}{H\beta}$ where *h* is Planck's constant, *v* is the operating frequency, *H* is the magnetic field and *β* is the Bohr magneton.

Electrochemical measurements: Electrochemical or cyclic voltammetry measurements were performed using a CHI-6205 electrochemical analyzer instrument. Tetrabutylammonium hexafluorophosphate (TBAP) was employed as the supporting electrolyte (0.1 M). The measurements were done using three-electrode configurations like Pt disk as the working electrode, Pt wire as the counter electrode and aqueous saturated Ag/AgCl as the reference electrode. The voltammograms were recorded keeping the potential window at −1.5 to 1.5 V and the scan rate as 100 mV/s.

238

Organic Materials O. Chatterjee et al. Original Article

Field emission scanning electron microscopy (FESEM) study: Samples for FESEM were prepared by drop-casting the samples on cover slips placed upon aluminium stub with the help of adhesive carbon tapes. The samples were further dried under vacuum overnight and coated with a thin layer of sputtered gold prior to imaging. High-resolution FESEM images were visualized using an Ultra Plus Zeiss instrument while keeping the working voltage as 20 kV.

Thin-film preparation: To construct the transparent thin film, PMMA polymer was added to the solution of **DIPFPDI** in $CHCl_3$ (0.5 mM) and stirred at room temperature for an hour to obtain a homogeneous solution. This solution was then drop-casted on a cleaned quartz plate, spin-coated on a spin-coater (Apex Instruments, model no. SPINNXG-P1-H) and dried properly in a hot air oven for 2 h at 60 °C.

DFT and TDDFT calculations: Geometry optimizations were performed for neutral **DIPFPDI**, radical anionic species and the corresponding dimers using DFT methodologies as implemented in Gaussian 16. We used long-range corrected density functional, CAM-B3LYP along with 6 – 311 G** basis sets, for all the atoms. For computing the spectral features of the species, we performed TDDFT calculations in DMF medium by employing a polarizable continuum model using the integral equation formalism variant (IEFPCM). We employed the Heyd–Scuseria–Ernzerhof exchange correlational functional (HSE06) for computing the absorption spectra.

Funding Information

Acknowledgements

Supporting Information

Supporting Information for this article is available online at https://doi.org/10.1055/a-1967-8617.

Conflict of Interest

The authors declare no conflict of interest.

References

(1) Whitesides, G. M.; Grzybowski, B. *Science* **2002**, *295*, 2418.

(2) van Rossum, S. A. P.; Tena-Solsona, M.; van Esch, J. H.; Eelkema, R.; Boekhoven, J. *Chem. Soc. Rev.* **2017**, *46*, 5519.

(3) (a) Mattia, E.; Otto, S. *Nat. Nanotechnol.* **2015**, *10*, 111. (b) Arango-Restrepo, A.; Barragán, D.; Rubi, J. M. *Phys. Chem. Chem. Phys.* **2019**, *21*, 17475.

(4) Goldbeter, A. *Philos. trans. R. Soc. London* **2018**, *376*, 20170376.

(5) (a) Nicolis G.; Prigogine, I. *Self-Organization in Nonequilibrium Systems: From Dissipative Structures to Order through Fluctuations*, 1st ed.; John Wiley: New York, **1977**. (b) Merindol, R.; Walther, A. *Chem. Soc. Rev.* **2017**, 46, 5588.

(6) Hess, H.; Ross, J. L. *Chem. Soc. Rev.* **2017**, *46*, 5570.

(7) (a) De, S.; Klajn, R. *Adv. Mater.* **2018**, *30*, 1706750. (b) Riess, B.; Grötsch, R. K.; Boekhoven, J. *Chem* **2020**, *6*, 552. (c) Ragazzon, G.; Prins, L. J. *Nat. Nanotechnol.* **2018**, *13*, 882. (d) Sharko, A.; Livitz, D.; De Piccoli, S.; Bishop, K. J. M.; Hermans, T. M. *Chem. Rev.* **2022**, *122*, 11759. (e) Leira-Iglesias, J.; Sorrenti, A.; Sato, A.; Dunne, P. A.; Hermans, T. M. *Chem. Commun.* **2016**, *52*, 9009. (f) Leira-Iglesias, J.; Tassoni, A.; Adachi, T.; Stich, M.; Hermans, T. M. *Nat. Nanotechnol.* **2018**, *13*, 1021.

(8) Boekhoven, J.; Brizard, A. M.; Kowlgi, K. N. K.; Koper, G. J. M.; Eelkema, R.; van Esch, J. H. *Angew. Chem. Int. Ed.* **2010**, *49*, 4825.

(9) Weißenfels, M.; Gemen, J.; Klajn, R. *Chem* **2021**, *7*, 23.

(10) Kathan, M.; Hecht, S. *Chem. Soc. Rev.* **2017**, *46*, 5536.

(11) Bian, T.; Chu, Z.; Klajn, R. *Adv. Mater.* **2020**, *32*, 1905866.

(12) (a) Nowak-Król, A.; Würthner, F. *Org. Chem. Front.* **2019**, *6*, 1272. (b) Roy, R.; Khan, A.; Chatterjee, O.; Bhunia, S.; Koner, A. L. *Org. Mater.* **2021**, *3*, 417.

(13) (a) Kumar, S.; Shukla, J.; Kumar, Y.; Mukhopadhyay, P. *Org. Chem. Front.* **2018**, *5*, 2254. (b) Sharma, V.; Puthumana, U.; Karak, P.; Koner, A. L. *J. Org. Chem.* **2018**, *83*, 11458. (c) Khan, A.; Agrahari, A.; Saha, S.; Koner, A. L. *J. Mater. Chem. C* **2022**, *10*, 14480.

(14) (a) Ghosh, I.; Ghosh, T.; Bardagi Javier, I.; König, B. *Science* **2014**, *346*, 725. (b) La Porte, N. T.; Martinez, J. F.; Hedström, S.; Rudshteyn, B.; Phelan, B. T.; Mauck, C. M.; Young, R. M.; Batista, V. S.; Wasielewski, M. R. *Chem. Sci.* **2017**, *8*, 3821.

(15) Lee, S.-H.; Oh, B. M.; Hong, C. Y.; Jung, S.-K.; Park, S.-H.; Jeon, G. G.; Kwon, Y.-W.; Jang, S.; Lee, Y.; Kim, D.; Kim, J. H.; Kwon, O. P. *ACS Appl. Mater. Interfaces* **2019**, *11*, 35904.

(16) Kumar, S.; Kumar, Y.; Keshri, S. K.; Mukhopadhyay, P. *Magnetochemistry* **2016**, *2*, 42.

(17) (a) Jiao, Y.; Liu, K.; Wang, G.; Wang, Y.; Zhang, X. *Chem. Sci.* **2015**, *6*, 3975. (b) Lü, B.; Chen, Y.; Li, P.; Wang, B.; Müllen, K.; Yin, M. *Nat. Commun.* **2019**, *10*, 767.

(18) (a) Sun, Z.; Zeng, Z.; Wu, J. *Acc. Chem. Res.* **2014**, *47*, 2582. (b) Chatterjee, O.; Roy, R.; Pramanik, A.; Dutta, T.; Sharma, V.; Sarkar, P.; Koner, A. L. *Adv. Opt. Mater.* **2022**, in press; doi: 10.1002/adom.202201187.

(19) Schmidt, R.; Oh, J. H.; Sun, Y.-S.; Deppisch, M.; Krause, A.-M.; Radacki, K.; Braunschweig, H.; Könemann, M.; Erk, P.; Bao, Z.; Würthner, F. *J. Am. Chem. Soc.* **2009**, *131*, 6215.

(20) Scholz, R.; Schreiber, M. J. C. P. *J. Chem. Phys.* **2006**, *325*, 9.

(21) Jiménez, Á. J.; Lin, M.-J.; Burschka, C.; Becker, J.; Settels, V.; Engels, B.; Würthner, F. *Chem. Sci.* **2013**, *5*, 608.

(22) (a) Giaimo, J. M.; Lockard, J. V.; Sinks, L. E.; Scott, A. M.; Wilson, T. M.; Wasielewski, M. R. *J. Phys. Chem. A* **2008**, *112*, 2322. (b) Yagai, S.; Usui, M.; Seki, T.; Murayama, H.; Kikkawa, Y.; Uemura, S.; Karatsu, T.; Kitamura, A.; Asano, A.; Seki, S. *J. Am. Chem. Soc.* **2012**, *134*, 7983.

(23) Gosztola, D. J.; Niemczyk, M. P.; Svec, W. A.; Lukas, A. S.; Wasielewski, M. R. J. J. o. P. C. A. *J. Phys. Chem. A* **2000**, *104*, 6545.

(24) Hestand, N. J.; Spano, F. C. *Chem. Rev.* **2018**, *118*, 7069.

(25) Clark, J.; Chang, J.-F.; Spano, F. C.; Friend, R. H.; Silva, C. *Appl. Phys. Lett.* **2009**, *94*, 163306.

(26) Grötsch, R. K.; Wanzke, C.; Speckbacher, M.; Angı, A.; Rieger, B.; Boekhoven, J. *J. Am. Chem. Soc.* **2019**, *141*, 9872.

(27) Meinardi, F.; Cerminara, M.; Sassella, A.; Bonifacio, R.; Tubino, R. *Phys. Rev. Lett.* **2003**, *91*, 247401.

(28) Guha, S.; Goodson, F. S.; Corson, L. J.; Saha, S. *J. Am. Chem. Soc.* **2012**, *134*, 13679.

(29) Goodson, F. S.; Panda, D. K.; Ray, S.; Mitra, A.; Guha, S.; Saha, S. *Org. Biomol. Chem.* **2013**, *11*, 4797.

(30) Frisch, M. J.; Trucks, G. W.; Schlegel, H. B.; Scuseria, G. E.; Robb, M. A.; Cheeseman, J. R.; Scalmani, G.; Barone, V.; Petersson, G. A.; Nakatsuji, H.; Li, X.; Caricato, M.; Marenich, A. V.; Bloino, J.; Janesko, B. G.; Gomperts, R.; Mennucci, B.; Hratchian, H. P.; Ortiz, J. V.; Izmaylov, A. F.; Sonnenberg, J. L.; Williams-Young, D.; Ding, F.; Lipparini, F.; Egidi, F.; Goings, J.; Peng, B.; Petrone, A.; Henderson, T.; Ranasinghe, D.; Zakrzewski, V. G.; Gao, J.; Rega, N.; Zheng, G.; Liang, W.; Hada, M.; Ehara, M.; Toyota, K.; Fukuda, R.; Hasegawa, J.; Ishida, M.; Nakajima, T.; Honda, Y.; Kitao, O.; Nakai, H.; Vreven, T.; Throssell, K.; Montgomery, J. A., Jr.; Peralta, J. E.; Ogliaro, F.; Bearpark, M. J.; Heyd, J. J.; Brothers, E. N.; Kudin, K. N.; Staroverov, V. N.; Keith, T. A.; Kobayashi, R.; Normand, J.; Raghavachari, K.; Rendell, A. P.; Burant, J. C.; Iyengar, S. S.; Tomasi, J.; Cossi, M.; Millam, J. M.; Klene, M.; Adamo, C.; Cammi, R.; Ochterski, J. W.; Martin, R. L.; Morokuma, K.; Farkas, O.; Foresman, J. B.; Fox, D. J. *Gaussian 16, Revision B.01*. Gaussian, Inc.: Wallingford, CT, **2016**.

(31) Oleson, A.; Zhu, T.; Dunn, I. S.; Bialas, D.; Bai, Y.; Zhang, W.; Dai, M.; Reichman, D. R.; Tempelaar, R.; Huang, L.; Spano, F. C. *J. Phys. Chem. C* **2019**, *123*, 20567.

(32) (a) Biswas, S.; Pramanik, A.; Pal, S.; Sarkar, P. *J. Phys. Chem. C* **2017**, *121*, 2574. (b) Biswas, S.; Pramanik, A.; Sarkar, P. *J. Phys. Chem. C* **2018**, *122*, 14296.

(33) Heyd, J.; Scuseria, G. E.; Ernzerhof, M. *J. Chem. Phys.* **2003**, *118*, 8207.